Materials Science & Engineering A 886 (2023) 145660

Contents lists available at ScienceDirect

Materials Science & Engineering A

journal homepage: www.elsevier.com/locate/msea

Influence of mean stress and overaging on fatigue life of aluminum alloy EN AW-2618A

Ying Han [a,*], Julius Kruse [a], Julian M. Rosalie [a], Jan Radners [b], Philipp von Hartrott [b], Birgit Skrotzki [a]

[a] Bundesanstalt für Materialforschung und -prüfung (BAM), Unter den Eichen 87, 12205, Berlin, Germany
[b] Fraunhofer-Institut für Werkstoffmechanik IWM, 79108, Freiburg, Germany

ARTICLE INFO

Keywords:
Aluminum alloys
Aging
Fatigue
Microstructure
Electron microscopy
S-phase

ABSTRACT

Fatigue tests were performed on the forged aluminum alloy EN AW-2618A in the T61 state. Different stress ratios (R = −1, R = 0.1) were selected to study the influence of mean stress on fatigue life. Two overaged states (10 h/230 °C, 1000 h/230 °C) were also tested to investigate the influence of overaging on fatigue life. Transmission electron microscopy (TEM) was used to characterize the precipitates (S-phase), which are mainly responsible for the strength of the alloy. A fractographic analysis was also performed to determine the failure mode. Overaging reduces the fatigue life compared to the T61 state. The longer the aging time, the lower the fatigue resistance. The reason is the decrease in (yield) strength, which correlates with the radius of the S-phase: the precipitate radius increases by a factor of approximately two for the overaged states compared to the initial state. The analysis of the fracture surfaces showed crack initiation occurs predominantly on the outer surface and is associated with the primary phases.

1. Introduction

The aluminum alloy EN AW-2618A (2618A) is a precipitation-hardened high strength alloy, which finds its application in the transportation and aerospace industries [1]. Due to its advantageous mechanical properties (e. g., long-term creep resistance), this alloy is mainly used for elevated temperature applications. The main alloying elements are Cu and Mg, but it also contains Fe and Ni. The latter elements form coarse constituent particles Al_9FeNi of several μm in size and cause dispersion hardening [2]. This so-called primary phase is formed during solidification [1]. Mg_2Si is present as a further primary phase [3]. In addition to the primary phases, the alloy also forms a hardening precipitate phase (S-phase), which is primarily responsible for the strength due to precipitation hardening. In the following this precipitate is referred to only as S-phase. The rod-shaped S-phase precipitates from the supersaturated solid solution (SSSS) during the heat treatment [4–7] with the equilibrium composition of Al_2CuMg [8]. For this phase the following precipitation sequence was proposed [9]:

$$\text{SSSS} \rightarrow \text{GPB zones} \rightarrow \text{S''} \rightarrow \text{S}$$

The GPB (Guinier-Preston-Bagaryatski) zones represent small clusters of solute atoms that have not yet taken the form of precipitates [10]. The transition phase S’’ is described as a metastable, slightly distorted variant of the stable S-phase [9]. In the following, the different variants of the S-phase will not be distinguished and will be referred to as S-phase. In contrast to the primary phases, the S-phase is not stable. It coarsens during further exposure at elevated temperatures, e. g., during component operation [3,11–13].

Lifshitz and Slyozov [14] as well as Wagner [15] described the coarsening of spherical precipitates quantitatively for the first time. This coarsening is also called Ostwald ripening. For cylindrical particles, the Ostwald ripening law needs to be modified [16]. Recently, Rockenhäuser et al. [13,17] have shown that the classic Ostwald ripening law cannot be applied for a quantitative description of the S-phase evolution under short-time aging or external load. The isothermal (190 °C) and load-free aging of 2618A in the T61 state was studied in Ref. [13]. Transmission electron microscopy (TEM) and differential scanning calorimetry (DSC) measurements were used to investigate the aging process up to 25000 h. The DSC measurements show a coexistence of GPB zones and S-phase for short aging times (<1000 h). Due to the change from the growth to the ripening stage at around 1000 h, the classical Ostwald ripening law does not describe the coarsening

---

* Corresponding author.
E-mail address: ying.han@bam.de (Y. Han).

https://doi.org/10.1016/j.msea.2023.145660
Received 7 August 2023; Received in revised form 1 September 2023; Accepted 2 September 2023

satisfactorily. Therefore, an approach was chosen that considers ripening only after the complete dissolution of the GPB zones.

Alloy 2618A is widely used for exhaust gas turbocharger compressor wheels. These components are typically forged and subjected to mechanical and thermal stresses during service. The air outlet and the back of the compressor wheel are highly stressed by creep and exposed to temperatures close to (or even higher than) the aging temperature that may cause material overaging and adversely affect the mechanical properties. The entire component is subjected to fatigue, due to speed changes as well as start-up and shut-down processes. To exploit the full potential of this alloy, and also in regard of lifetime simulations, it is necessary to have a comprehensive knowledge of the fatigue resistance for relevant (over-) aging and microstructural states.

The fatigue behavior of alloy 2618A has been studied occasionally in the low cycle (LCF) [18,19] and high cycle (HCF) [20] ranges. The focus was predominantly on room temperature (RT), although the alloy is intended for use at elevated temperature. There is little literature on the influence of overaging on the fatigue resistance of 2618A, especially for aging temperatures above the hardening temperature (190 °C–195 °C).

For the alloy RR58 (which is the British brand name for 2618A [21]), the low cycle fatigue (LCF) behavior of different aging conditions was investigated by Malakondaiah et al. [18] and Singh et al. [19]. The tests were performed at 20 °C and 150 °C. The authors compared a slightly overaged condition (OA; 72 h/190 °C), an underaged condition (UA; 3 h/190 °C) and a peak aged condition (PA; 15 h/190 °C). The OA state showed a longer fatigue life than the UA state for both 20 °C and 150 °C. The material in the PA state showed an intermediate behavior [18]. The authors observed that the different thermal treatments result in different microstructures and the varying microstructures directly affect the fatigue resistance. The characteristics of the microstructure and the type of phases present were revealed using transmission electron microscopy (TEM): GPB zones were found in the UA condition, a mixture of GPB zones and intermediate S'-phase precipitates in the PA condition, and uniformly distributed coarse equilibrium S precipitates in the OA state. The UA condition which shows the lowest fatigue life is characterized by fine, unevenly distributed, unstable and penetrable GPB zones. The OA condition shows the highest fatigue resistance, and this is associated with the presence of uniformly distributed, stable and impenetrable S precipitates. The authors state that these precipitates are the most stable of all conditions tested. They remain stable even during cyclic loading [19].The test temperature has no significant effect on the fatigue life and failure mode.

Finney [20] performed high cycle fatigue (HCF) tests up to 10^8 cycles at 20 °C on the same alloy. The influence of aging (UA: 4 min, PA: 7 h, OA: 720 h) at a temperature of 200 °C was studied. The results show that the fatigue resistance decreases in the following order: PA, UA, OA condition. Note that the results of the PA and UA conditions differ only slightly. The fractographic examinations show that for the UA condition, cracks initiate and propagate in the micro-shear mode. Failure in the PA condition initiates in the micro-shear mode, followed by tensile mode failure. The failure of the OA condition is completely in the tensile mode. Finney reports that the failure mode is related to the surface deformation characteristics: All conditions (PA, UA) where slip band deformation during fatigue was observed, failed in shear mode. In contrast, the OA state exhibits grain boundary deformation. The failures due to unimpeded discrete slip band fatigue surprisingly show the highest fatigue resistance. Finney concludes that shearing of the precipitates is not harmful in terms of fatigue resistance but suggests the opposite: structures with coherent easy to shear precipitates, have a higher fatigue resistance than the overaged condition with much larger precipitates.

Health-Smith et al. [22] have performed fatigue tests at room temperature on two overaged states (1000 h/150 °C and 30000 h/120 °C) of RR58. The results show, that the overaging has only little effect on the fatigue performance. Apparently, the temperatures are too far below the hardening temperature of 195 °C to cause mechanical degradation.

This summary shows that there have been some investigations of the low and high cycle fatigue behavior of 2618A at room temperature, and that the influence of pre-aging has also been considered. However, the aging temperatures (with the exception of Finney's work [20]) were generally well below the hardening temperature, at which aging processes are hardly or not yet to be expected. Likewise, the influence of aging for application-relevant temperatures and times has not yet been sufficiently taken into account. Since operating temperatures of >200 °C are the target for radial compressor wheels, at least for short periods of time, overaging conditions in this temperature range must also be considered. However, no published results are currently available for such states. Therefore, the focus of this work is on the high cycle fatigue behavior of two overaged conditions at 230 °C and the comparison with the initial T61 state.

2. Material and method

The material under investigation was manufactured from forged cylindrical blanks (Fig. 1a) from the aluminum alloy EN AW-2618A in the T61 state, which is a slightly underaged condition. The heat treatment consists of a solution annealing at 530 °C for 8 h followed by quenching in boiling water and hardening at 195 °C for 28 h followed by air-cooling to ambient temperature. The chemical composition of the material used is given in Table 1.

The cylindrical blanks which are the semi-finished products for the manufacturing of radial compressor wheels were divided into four sections (Fig. 1b). The specimens for uniaxial fatigue testing were taken from section 3 (Fig. 1c) because this is the area of the final component expected to experience fatigue loading. Rectangular blocks measuring 16 mm × 16 mm × 100 mm were cut out from section 3 (Fig. 1d). Depending on the test state, the rectangular blocks were either machined directly (T61 state) or aged before being machined to their final shape (see Fig. 2). After aging, the rectangular blocks were cooled in air. The fatigue tests were performed on the as-received T61 state and on two overaged states: T61 + 10 h/230 °C and T61 + 1000 h/230 °C (in the following designated as 10 h/230 °C and 1000 h/230 °C, respectively). Since the overaging temperature (230 °C) is much higher than the hardening temperature (195 °C), microstructural changes were expected in terms of S-phase precipitate size.

Prior to the fatigue test, the gauge length of the specimens was polished with a highly concentrated diamond compound with a grain size of 25 μm, while polishing paraffin oil was used as a lubricant resulting in an average roughness of $R_z \approx 0.4$ μm. The objective was to establish a roughness comparable to that of the component (radial compressor wheel) after machining.

All fatigue tests were performed on a SCHENCK HYDROPULS PSB servo-hydraulic closed-loop controlled machine calibrated to DIN EN ISO 7500-1 [24] and aligned according to ISO 23788 [25]. The fatigue tests presented in this paper were conducted at room temperature (RT), with a test frequency of 20 Hz, a sinusoidal waveform, and force-controlled according to DIN 50100 [26].

The results of the fatigue test were performed and evaluated according to DIN 50100, using the pearl string method. According to this method, at least one specimen is tested at each stress amplitude. In general, the specimens were tested until failure. However, in some cases the test was stopped before failure. These cases are referred to as run-outs. According to DIN 50100, aluminum specimens sustaining 10^7 cycles without failure were not included in the S–N curve evaluation. Prior to evaluation, the data points were examined using the Grubbs test to detect potential outliers and to exclude them if necessary. The S–N curves are commonly described by equation (1) [26], where σ_a is the stress amplitude, N is the number of cycles to failure, C is the intercept for N with $\sigma_a = 1$, and k is the slope of the curve in a double logarithmic plot.

$$N = C \bullet \sigma_a^{-k} \tag{1}$$

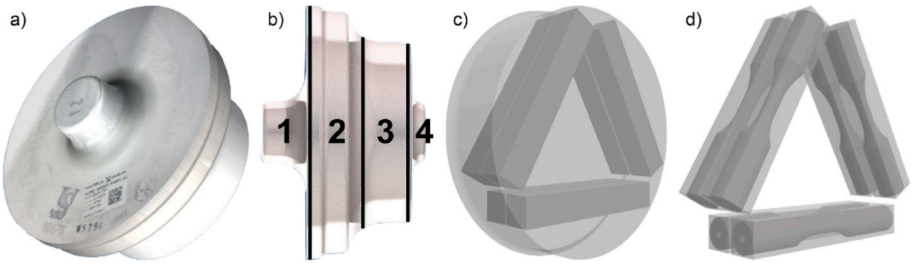

Fig. 1. Sampling: a) Forged round blank, b) Blank divided into four sections, c) Orientation of rectangular blocks in section 3, d) Rectangular blocks (16 mm × 16 mm × 100 mm), from which specimens were extracted.

Table 1
Analyzed chemical composition (wt.%) of EN AW-2618A.

Element	Cu	Mg	Fe	Ni	Si	Mn	Zn	Ti	Cr	Al
Min.[a]	1.80	1.20	0.90	0.80	0.15				–	
Max.[a]	2.70	1.80	1.40	1.40	0.25	0.25	0.15	0.20	–	
Inspection certificate	2.50	1.60	1.10	1.10	0.23	<0.10	<0.10	0.05	<0.01	BAL

[a] According to DIN EN 573-3 [23].

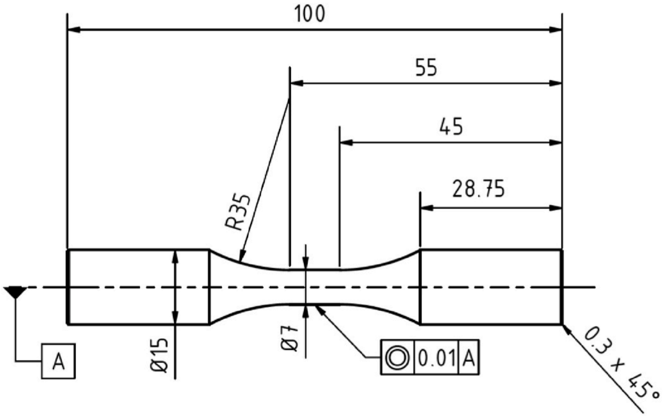

Fig. 2. Geometry of the fatigue specimen. Dimensions in mm, depiction not true to scale.

Two sets of tests were conducted. The first one studies the influence of mean stress. The mean stress is defined as [27]:

$$\sigma_m = \frac{\sigma_{max} + \sigma_{min}}{2} \tag{2}$$

where σ_{max} is the maximum stress and σ_{min} is the minimum stress during a single cycle. It is also often described by the stress ratio R, which is defined as [26]:

$$R = \frac{\sigma_{min}}{\sigma_{max}} \tag{3}$$

The investigation of the influence of the mean stress was performed in the T61 state and with two different stress ratios ($R = -1$, $R = 0.1$), i.e., with mean stress zero as well as with positive mean stress). For comparability, the stress ratio $R = -1$ was chosen because it is commonly found in the literature. The stress ratio $R = 0.1$ was selected because it often occurs in fatigue dominated areas of the component.

The second set of tests investigates the influence of overaging. For this purpose, tests were performed on overaged material states (10 h/230 °C, 1000 h/230 °C).

The Brinell hardness HBW 2.5/62.5 according to DIN EN ISO 6506-1 [28] was measured after aging at 230 °C for different times. After aging the samples were cooled in water at room temperature. The hardness was determined on square samples (30 mm × 30 mm) with a thickness of 4 mm using the Emco Test M4C 025 G3 hardness tester. The measurement uncertainty of all specimens is max. ± 7 HBW 2.5/62.5.

To determine the mechanical properties, tensile tests were performed following DIN EN ISO 6892-1 [29]. These tests were performed at room temperature and with a constant strain rate of 10^{-4} s^{-1}. The 10 h/230 °C state was tested on a Zwick Kappa 100 SS with the geometry shown in Fig. 3a. A Maytec PMA 12 extensometer calibrated to DIN EN ISO 9513 [30] was used to measure the strain. The 1000 h/230 °C state was tested on an Instron 8861 testing machine with the geometry shown in Fig. 3b. For this test a similar extensometer calibrated to the aforementioned standard was used for strain measurement. One test piece was tested for each overaged state. Tensile strength R_m, proof strength $R_{p0.2}$, percentage strain after fracture A_5, and percentage reduction of

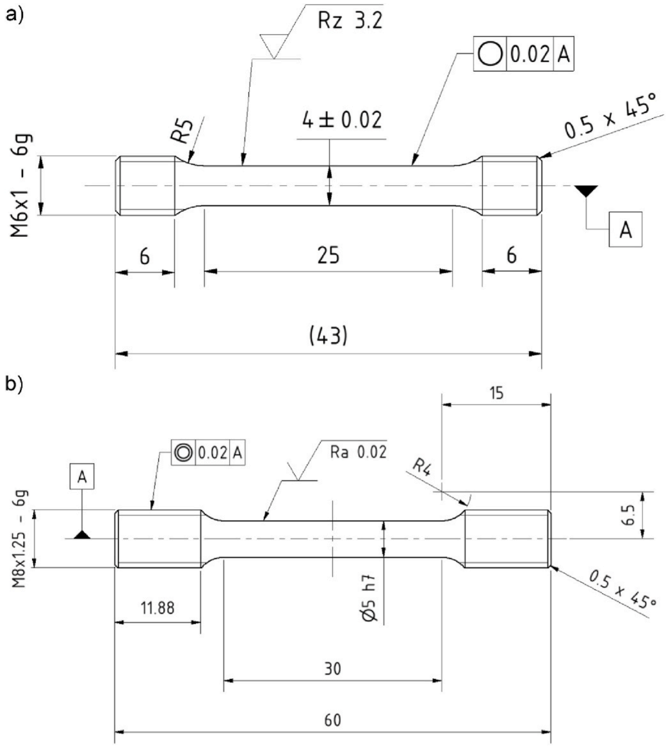

Fig. 3. Geometry of tensile test pieces. Dimensions in mm, depiction not true to scale.

area Z were determined. The characteristic strength values allow a rating of the selected maximum stresses of the fatigue tests as well as an evaluation whether plastic deformation has to be expected.

Light optical microscopy investigations were carried out on microsections, which were extracted from the clamping section of the tested HCF specimens. For metallographic preparation, the extracted material was embedded in epoxy resin. The microsections were ground and polished using Struers TregrapPol-11 with a TegraForce attachement. Abrasive paper with grits of 600, 1200 and 4000 were used for grinding. Grinding with grit of 600 and 1200 was performed for 30 s each, while grinding with grit 4000 was performed for 20 s each. The loads were 20 N (grit 600) and 15 N (grit 1200 and 4000). Diamond paste with a grit size of 3 μm and 1 μm was used for polishing. Here, the loads were 20 N (grit 3 μm) and 15 N (grit 1 μm). For cleaning, polishing was performed with water for 30 s at a load of 15 N. Grinding and polishing were carried out in a circular motion with 200 revolutions per minute. To make the grain boundaries visible, the microsections were etched for 8 s–10 s with caustic soda (30 %) heated to 60 °C. An Olympus GX71 light microscope was used for documentation.

Fractography was performed to gain a better understanding of the failure mode. For this purpose, a Tescan Vega 3 XLH scanning electron microscope (SEM) was used. It was operated with a tungsten hairpin cathode and the accelerating voltage was 20 kV. The images were taken using backscattered electrons (BSE) and secondary electrons (SE). BSE provides a better elemental contrast, while SE provides a better topography contrast.

Transmission electron microscopy (TEM) was used to characterize the S-phase. The aim is to determine the average radii of the studied material states. A JEM 2200FS with a field-emission gun operating at 200 kV was used. The TEM samples were prepared conventionally. First, 200–300 μm thick slices were cut perpendicular to the loading direction of the clamp section of the tested HCF specimens. These were then ground to a uniform thickness of 100–150 μm. Disks with a 3 mm diameter were then punched out and electropolished to electron transparency using a Struers Tenupol-3 twin-jet electropolisher. The electrolyte used was two parts pure methanol and one part nitric acid (65 %) cooled to – 20 °C with an applied voltage of 13 V. Dark-field transmission electron microscopy (DFTEM) was used for the study, with the grains oriented along the $[001]_\alpha$ axis. The procedure described in Refs. [13,17] was used as a guide for the TEM investigations. The DFTEM images were the basis to determine the average radii of the S-phase rods. ImageJ was used to analyze the DFTEM images and determine the effective particle area A. Then the effective particle area was used to calculate the equivalent particle radius r (S-phase considered as cylindrical rods):

$$r = \sqrt{\frac{A}{\pi}} \tag{4}$$

The processing of the images for the evaluation and calculation of the radii was also done according to Refs. [13,17]. A minimum of 300 particles per material state were evaluated. The lognormal function (equation (5)) was used to describe the distribution of the radii.

$$\mathrm{n(r)} = \frac{1}{\sqrt{2\pi}\mathrm{r}\sigma_{\mathrm{geo}}} \bullet \exp\left(-\frac{\left(\ln\left(\frac{\mathrm{r}}{\mathrm{r_m}}\right)\right)^2}{2\sigma_{\mathrm{geo}}^2}\right) \tag{5}$$

With particle radius r, median particle radius r_m, and the geometric standard deviation σ_geo. Based on the distribution, the average particle radius (r_a) was calculated using equation (6) [31].

$$r_\mathrm{a} = r_\mathrm{m} \bullet \exp\left(\frac{\sigma_\mathrm{geo}^2}{2}\right) \tag{6}$$

The T61 state data from Rockenhäuser et al. [13,17,32] were used to validate the evaluation and calculation of the radii.

3. Results

3.1. Mechanical properties

Tensile tests were performed to obtain information on the mechanical properties of both overaged states. The properties of the initial T61 state were taken from the supplier's inspection certificate. The test temperature T for the tensile tests was room temperature. The results of the tensile tests and hardness measurements of the three tested states are shown in Table 2. Note, that the values for the overaged states reported in Table 2 refer to the results of a single test. Nevertheless, the scatter is expected to be negligible as shown for the T61 state. The proof strength ($R_{\mathrm{p}0.2}$), ultimate tensile strength (R_m), and hardness (HBW 2.5/62.5) decrease with increasing aging time.

3.2. Fatigue behavior

3.2.1. Influence of mean stress on fatigue life

Fig. 4 shows the fatigue test results obtained at the stress ratios $R = -1$ (solid squares) and $R = 0.1$ (open squares) in the T61 state. The fit of the S–N curve is shown by a solid line, which represents the 50 % failure probability ($P_{\mathrm{A},50\%}$). Runouts are marked with triangles. It is noted that the highest stress amplitude of the tests at $R = 0.1$ results in maximum stresses σ_max above the proof strength $R_{\mathrm{p}0.2}$. The S–N curve was also evaluated without the highest stress amplitude. Since there is little difference in the slope of the S–N curves, it was decided to include the highest stress amplitude in the evaluation. For the tests at $R = -1$, all stresses were below the proof strength. It can be observed that the tests at $R = -1$ have a longer fatigue life than the tests at $R = 0.1$ with the same stress amplitude. For example, referring to the stress amplitude $\sigma_\mathrm{a} = 160$ MPa, the fatigue life of the S–N curves differs by two orders of magnitude. The fit parameters of the S–N curves according to equation (1) are summarized in Table 3. The slope (k) of both curves is comparable, although the S–N curve for the $R = -1$ tests is slightly steeper.

3.2.2. Influence of overaging on fatigue life

Fig. 5 shows the S–N curves of the overaged states compared to the T61 state. The results of the 10 h/230 °C state are represented by half-filled dark blue squares and those of the 1000 h/230 °C state by half-filled light blue squares. Runouts are marked with triangles. Note that for both overaged states the two highest stress amplitudes cause maximum stresses σ_max above the proof strength $R_{\mathrm{p}0.2}$. The data points of all stress amplitudes were evaluated for a better confidence level. The S–N curve of the 1000 h/230 °C state show a lower fatigue life (approx. by a factor of four) than the S–N curve of the 10 h/230 °C state. Both S–N curves have approximately the same slope. The fit parameters of the S–N curves are summarized in Table 3. Of the three material states shown, the initial T61 state has the highest fatigue life. It can be seen from the diagram that the fatigue life decreases as the aging time increases. The T61 state has the steepest slope of the three S–N curves shown.

Table 2
Mechanical properties for the T61, 10 h/230 °C and 1000 h/230 °C state.

State	T [°C]	$R_{\mathrm{p}0.2}$ [MPa]	R_m [MPa]	A_5 [%]	Z [%]	HBW 2.5/62.5
T61[a]	RT	371 ± 3	421 ± 3	7 ± 1	10 ± 1	137 ± 2
10 h/230 °C	RT	302	370	6.5	12.0	115 ± 2
1000 h/230 °C	RT	265	351	7.1	10.0	105 ± 1

[a] The mechanical properties are an average of five individual values.

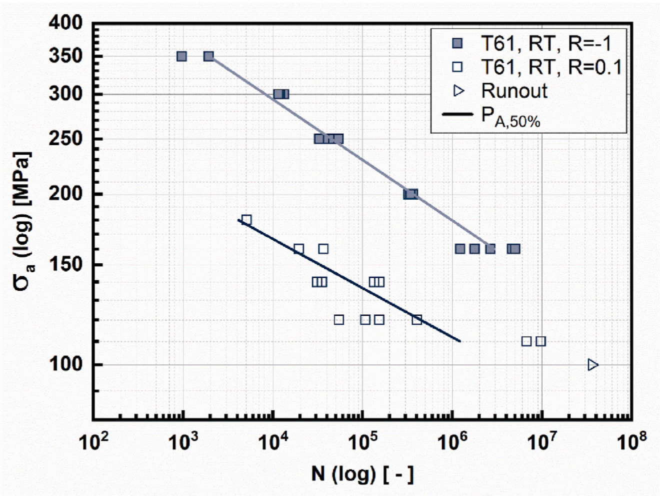

Fig. 4. S–N curves at room temperature for the T61 state with stress ratios $R = -1$ and $R = 0.1$.

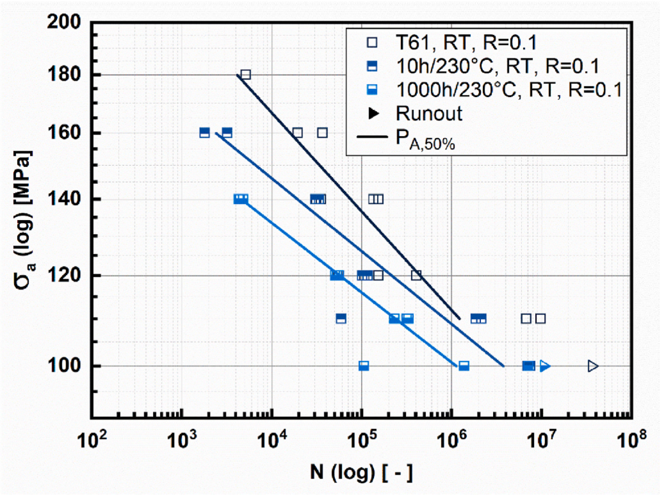

Fig. 5. S–N curves for $R = 0.1$ at room temperature for different aging states.

Table 3
Fit parameters (C, k) of the S–N curves shown in Figs. 4 and 5.

State	*T*	*R*	*C*	*k*
T61	RT	−1	$1.2\ 10^{27}$	9.4
T61	RT	0.1	$4.8\ 10^{29}$	11.6
10 h/230 °C	RT	0.1	$7.9\ 10^{37}$	15.7
1000 h/230 °C	RT	0.1	$6.3\ 10^{38}$	16.4

3.3. *Microstructure*

3.3.1. *Light microscopy*

The grain structure was investigated to see if overaging affects the grain size or the primary phases and thus, contributes to the degradation of the mechanical properties. The axial-radial plane of the three investigated states are shown in Fig. 6. The light grey lines are the grain boundaries, and the darker particles are the primary phases. They are arranged in planes as a result of the forging process. The average grain size of the three material states was determined by the linear intercept method according to DIN EN ISO 643 [33]. One observation field was analyzed per material state. In the selected observation field, a minimum of 50 line intersections with grain boundaries were evaluated. The following average grain sizes were measured: T61: 39 μm, 10 h/230 °C: 37 μm, 1000 h/230 °C: 41 μm. The results show that aging does not affect the microstructure on the microscale. No coarsening of either the grains or the primary phases was observed.

3.3.2. *Fractography*

The fracture surfaces of the specimens in the T61 state tested at $R = -1$ and $R = 0.1$ and at different stress amplitudes were examined to determine the crack features. The purpose of these examinations is to determine if there are differences in the crack initiation for different stress ratios. The fracture surfaces examined all look very similar. Therefore, a specimen tested at $\sigma_a = 250$ MPa and $R = -1$ is shown as an example. The images shown are taken in BSE mode (Fig. 7). The primary phases appear light/white, while the aluminum matrix appears grey. Fig. 7a shows the crack initiation region (yellow arrow), which is at the bottom of the image. A higher magnification of the crack initiation region is shown in Fig. 7b. In the latter image the specimen is slightly tilted. The lower part of the image shows the outer surface of the specimen, and the upper part shows the fracture surface. No secondary cracking was observed on the outer surface in the immediate vicinity of the crack initiation. Most cracks initiated at or just below the outer surface. Crack initiation from the interior of the specimen was the exception. The fractographic analyses indicate that the primary phases are involved in the crack initiation. In most cases, primary phases were observed in the immediate vicinity of the crack initiation. Furthermore, the crack initiation region shows facets. In general, the fatigue fracture region is transgranular and has a flat faceted appearance.

The fracture surfaces of the overaged states were also examined. The examined fracture surfaces of the two overaged states look very similar. Therefore, exemplary images of the 1000 h/230 °C state tested at $\sigma_a = 100$ MPa and $R = 0.1$ are shown in Fig. 8. These two images were taken in BSE mode. Fig. 8a show the crack initiation region. The outer surface with the crack initiation region of the slightly tilted specimen can been seen in Fig. 8b. The top of the image shows the fracture surface, and the rest of the image shows the outer surface of the specimen. The vertical lines on the outer surface are the polishing grooves. There are no secondary cracks on the outer surface visible. The fracture surfaces of the overaged states tested at stresses below the proof strength are indistinguishable from the fracture surfaces of the T61 state. As with the T61 state, the fatigue fracture region is transgranular and the crack initiates at or just below the outer surface. Again, in most cases primary phases were observed in the immediate vicinity of the crack initiation.

From the fractographic studies, it can be concluded that the fracture surfaces examined in the T61 state have the same fracture pattern. Therefore, it is assumed that there is no dependence between failure mode and stress ratio. The studies on the overaged states also suggest that there is no dependencc between failure mode and overaging for the tests performed at stresses below the proof strength.

3.3.3. *Transmission electron microscopy*

The three investigated material states were examined by means of TEM to analyze the size of the S-phase in the T61 and in the overaged states. The results of these investigations are shown in Fig. 9 which are DFTEM images, each obtained using a **g**-vector of type ½ <220>. The bright areas are the S-phase oriented along the $[001]_\alpha$ direction and penetrate the image plane. The T61 state shows the highest number of S-phase and the smallest size. The two overaged states have a smaller density of S-phase. However, their size is larger compared to the T61 state. From a casual inspection, it is not clear whether there is a difference in the size (i.e., radii) of the S-phase in the 10 h/230 °C and 1000 h/230 °C states. Therefore, the TEM images were used as a basis for the quantitative determination of the average radius of the S-phase. The results of this analysis are presented in Table 4. The quantitative analysis showed that the average radius, r_a, increased with aging time. Compared to the initial T61 state, the average radius of the 1000 h/230 °C state has more than doubled.

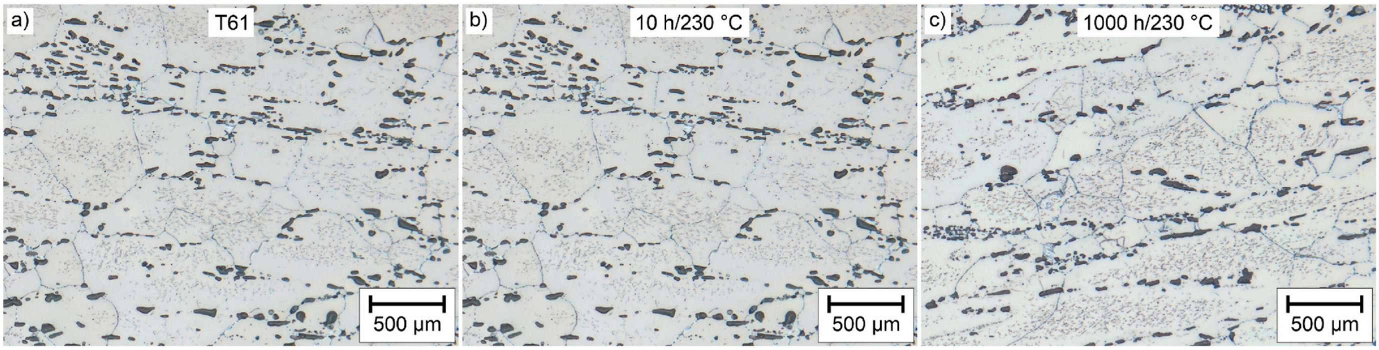

Fig. 6. Microstructure of the investigated material states: a) T61, b) 10 h/230 °C, c) 1000 h/230 °C.

4. Discussion

4.1. Influence of mean stress on fatigue life

Our results presented in section 3.2.1 show a clear detrimental effect of the mean stress on fatigue life for the T61 state which becomes more pronounced with longer aging. Malek et al. [34] investigated the fatigue behavior of 2618 in the T851 state and they also observed a decrease in fatigue life for higher stress ratios. It is well known that fatigue life decreases with increasing stress ratio, i.e., with rising mean stress level [10,35–37]. This is due to the type of loading: The stress is completely reversed for $R = -1$ [37], alternating between a maximum tensile and a minimum compressive stress of the same magnitude [36]. In contrast, the stress ratio $R = 0.1$ is a fluctuating tension loading [27], where the maximum and minimum stresses are asymmetric with respect to the zero stress level [36]. Thus, a higher mean stress results in a higher maximum stress for the same stress amplitude. This is illustrated in Fig. 10, where the results are plotted as maximum stress ($\sigma_{\max}$) instead of the stress amplitude vs. number of cycles to failure (N). Otherwise, the presentation of the results is the same as in Fig. 4 (solid squares for $R = -1$ and open squares for $R = 0.1$). The maximum stress is calculated as follows [26]:

$$\sigma_{\max} = \frac{2 \bullet \sigma_a}{(1-R)} \tag{7}$$

Comparing Figs. 4 and 10, it is clear, that the S–N curve of $R = -1$ has remained unchanged. However, the S–N curve of $R = 0.1$ now lies to the right of the curve for $R = -1$ when $\sigma_{\max}$ vs. N is plotted. For the stress ratio $R = -1$, the stress amplitude (e. g., $\sigma_a = 160$ MPa) corresponds to the maximum stress ($\sigma_a = \sigma_{\max}$), whereas the maximum stress at $R = 0.1$ is $\sigma_{\max} = 356$ MPa for the same stress amplitude. This has a more damaging effect on fatigue life. In addition, the higher the stress ratio at a given stress amplitude the longer the crack tip is open during the stress cycle [38]. For crack growth to occur, the crack tip must be fully open [10]. Therefore, the part of the cycle that contributes to crack propagation is greater for $R = 0.1$ than for $R = -1$.

Fig. 11 compares the results of the present study to literature data. All data generated at $R = -1$ are shown with dashed lines and the data generated at $R = 0.1$ are represented by solid lines. For the literature data, the S–N curves (using linear regression) and the corresponding data points were plotted, for the data of the present study only the fitted lines were plotted. It can be seen, that the results presented for the T61 state and $R = -1$ fit well with the data from Günther et al. [39] and Kaufmann [40]. No data could be found for the tested alloy with the stress ratio $R = 0.1$, neither for the T61 nor for the overaged states. Kaufmann [40] performed fatigue tests with $R = 0$ on 2618 in the T651 state. As expected, this data lies between the presented data for $R = -1$ and $R = 0.1$ in the T61 state.

4.2. Influence of overaging on fatigue

High-strength aluminum alloys obtain their strength by precipitation hardening. Setting the optimum mechanical properties requires defined combinations of temperature and time to achieve the desired size, number, and distribution of precipitates. The microstructure of precipitation-hardened aluminum alloys plays a fundamental role for their strength since only materials with the targeted microstructure achieve the desired strengths. However, in applications such as radial compressor wheels, this optimized microstructure may change during operation, because the components are used at temperatures near or above the hardening temperature. This process leads to a deterioration in strength (and hardness) over time and is undesirable. To assess the extent of microstructural changes and quantify their effect on fatigue behavior, two overaged states were investigated in the present study.

As expected, the results of the hardness measurements and tensile tests on the overaged states show a degradation of the mechanical properties, which is more pronounced for the longer aging time of 1000 h/230 °C. The fatigue tests show a shorter fatigue life for the longer aging at the same stress amplitude. These observations can be attributed to the coarsening of the S-phase, which was demonstrated by the TEM investigations (Table 4). The analyses showed the largest average radii for the 1000 h/230 °C state. Finely distributed S-phase act as obstacles for dislocations and make their movement more difficult [1,35]. During the coarsening process, the interparticle distance increases and the particle number density decreases for a given volume fraction of precipitates, because larger particles tend to grow at the expense of smaller ones [10]. According to the Orowan equation (8), this lowers the mechanical strength [1]:

$$\Delta\Gamma = 2\left\{\frac{Gb}{4\pi\sqrt{1-\nu}}\right\}\left\{\frac{1}{\lambda}\right\}\left\{ln\frac{D}{r_0}\right\} \tag{8}$$

$\Delta\Gamma$ is the increment in critical resolved shear stress due to dispersion strengthening, ν is the Poisson's ratio, G is the shear modulus, b is the Burgers vector of the gliding dislocation, λ is the effective inter-particle spacing, D is the planar diameter of the precipitate particles and r_0 is the core radius of the dislocation.

The observed coarsening is in good agreement with Rockenhäuser et al. [13]. They studied the coarsening of the alloy 2618A at 190 °C for different aging times (up to 25000 h) by TEM and quantified the radius of the S-phase. Fig. 12 shows the results from Ref. [13] together with those from the present work. The average particle radius r_a is plotted against aging time. The results of Rockenhäuser et al. [13] showed a rapid increase of the initial average radius due to the initial growth kinetics of the precipitates. Comparing the results of both studies, it is noticeable that the presented r_a for 0 h aging time ($r_a = 2.13$ nm) is slightly larger than that of Rockenhäuser et al. ($r_a = 1.79$ nm). It should be noted that the two studies investigated different batches, which could explain these small differences. On the other hand, it must also be acknowledged that quantitative microstructural analysis, even with the

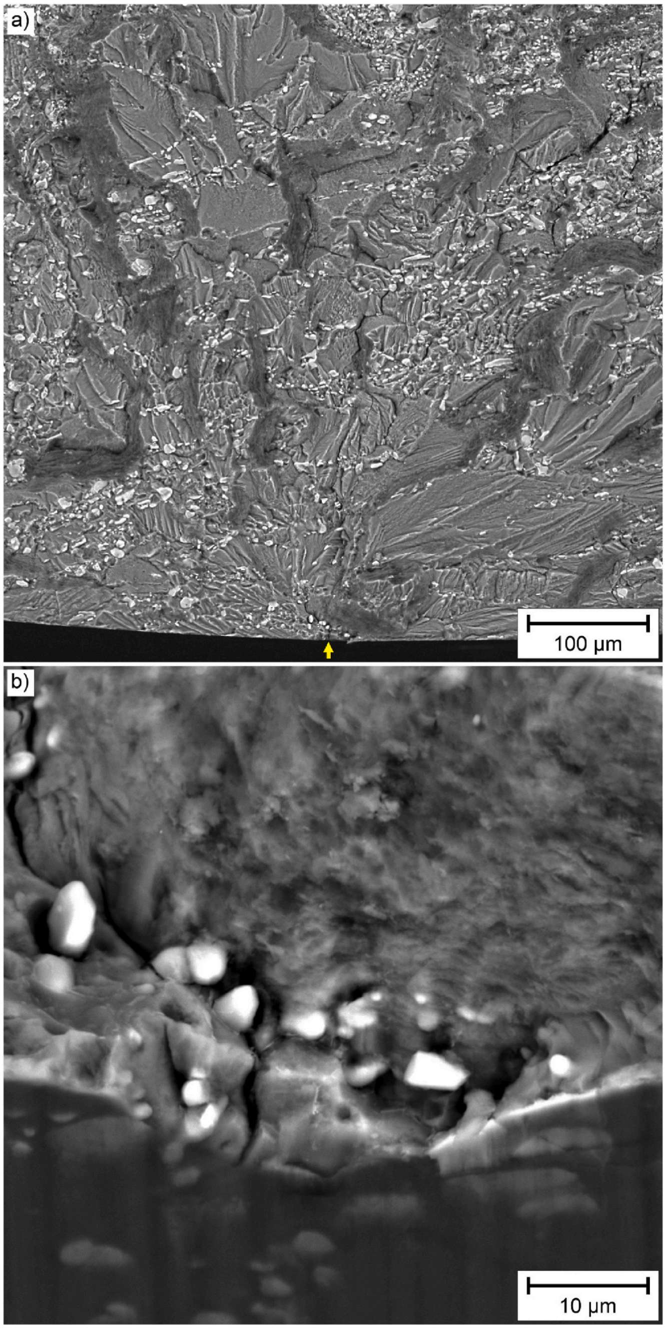

Fig. 7. SEM micrographs in BSE mode of fatigue fracture surface (T61, RT, $R = -1$, $\sigma_a = 250\ MPa$): a) Crack initiation region, c) High magnification of crack initiation region of tilted specimen, which shows the crack initiation.

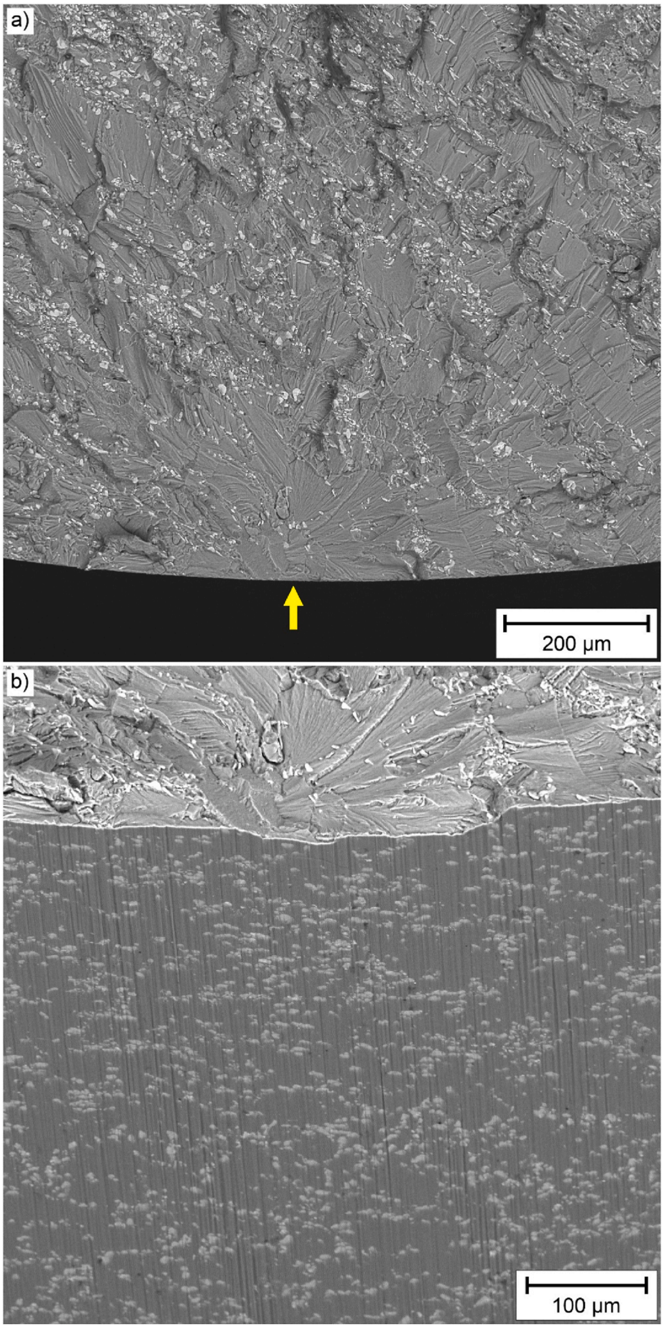

Fig. 8. SEM micrographs in BSE mode of overaged state (1000 h/230 °C, RT, $R = 0.1$, $\sigma_a = 100\ MPa$): a) Crack initiation region, b) Outer surface with the crack initiation region, specimen slightly tilted.

greatest care, always involves a certain human factor. The latter was taken into account by first evaluating the images of the T61 state from [13,17] in order to validate the procedure.

It is also noteworthy that r_a for an aging time of 1000 h at 190 °C is similar to that of the 10 h/230 °C state. This suggests that GPB zones are no longer present in the 10 h/230 °C state. For an aging time of 5000 h at 190 °C an average particle radius of $r_a = 5.50$ nm was measured, which is approximately the same as for the 1000 h/230 C state. This clearly demonstrates the significant acceleration of the coarsening processes at the 35 °C higher aging temperature. As a result of the coarsening a decrease in the hardness is observed [13].

Thus, the microstructure results can plausibly explain the fatigue life for the investigated material conditions: The S-phase coarsens rapidly during aging at 230 °C. The radius increases as well as the interparticle spacing λ, so that the strength contribution according to Eq 8 decreases more strongly for 1000 h than for 10 h. Consequently, the lower strength of the 1000 h/230 °C state results in a lower fatigue life than aging for the shorter aging time at the same temperature.

4.3. *Role of primary phases*

All microstructural features that lead to stress concentrations or that distribute plastic strain inhomogeneously may have a negative effect on fatigue life. In Al alloys, these include, for example, shearable precipitates and particle-free zones (PFZ) at grain boundaries. Primary phases also act as strain concentrators and can lead to early cracking. In

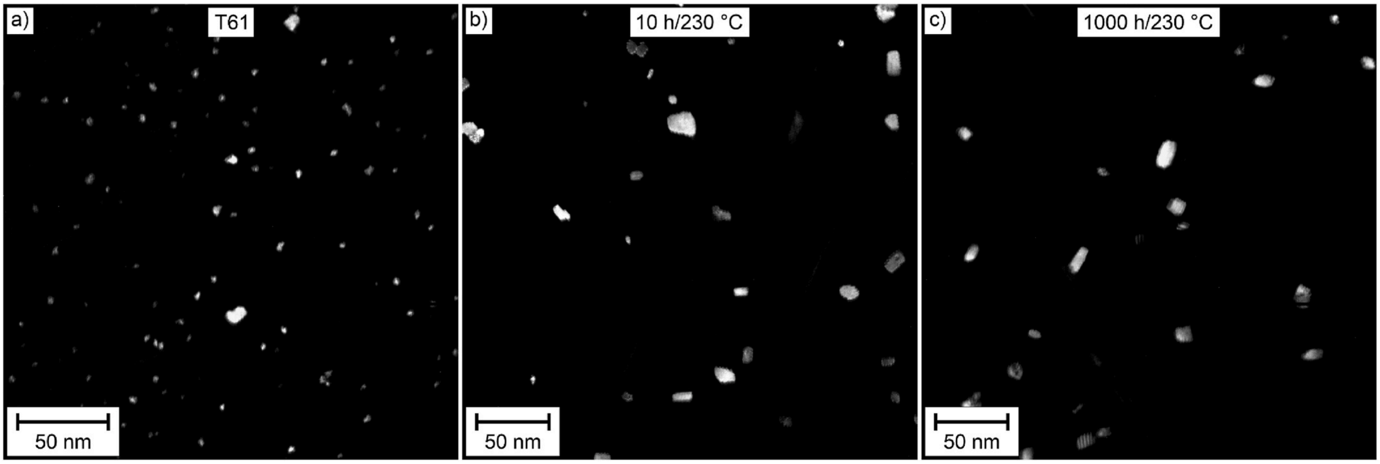

Fig. 9. DFTEM micrographs of the S-phase: a) T61, b) 10 h/230 °C, c) 1000 h/230 °C.

Table 4

Results of the quantitative radii determination of the S-phase for the T61 and the overaged states, r_m = resulting median particle radius, σ_{geo} = geometric standard deviation, r_a = average particle radius.

State	r_m [nm]	σ_{geo} [−]	r_a [nm]
T61	1.83 ± 0.12	0.56 ± 0.04	2.13 ± 0.12
10 h/230 °C	3.41 ± 0.44	0.83 ± 0.09	4.80 ± 0.44
1000 h/230 °C	5.16 ± 0.31	0.44 ± 0.05	5.68 ± 0.31

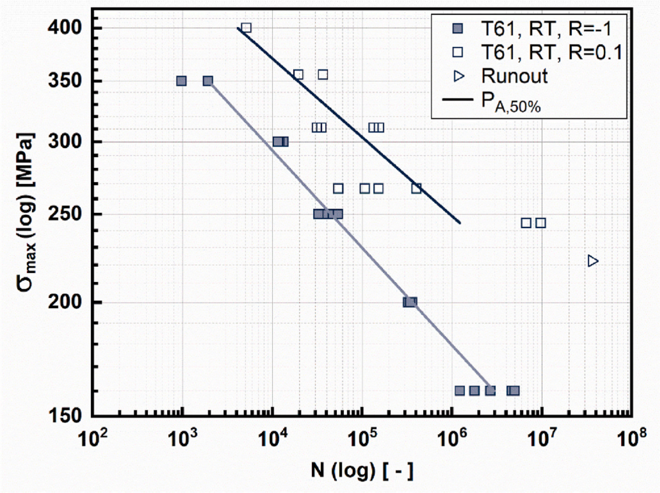

Fig. 10. S–N curves at room temperature with variation in stress ratio R, which are plotted as stress maximum σ_{max} vs. no. of cycles to failure N.

strain-controlled LCF experiments, constitutional phases containing iron and silicon as impurities (e.g., Al_7Cu_2Fe, $Al_{12}Fe$, Mn_3Si, Mg_2Si) and phases also formed as a result of alloy excess (e.g., Al_2Cu, Al_2CuMg) have been shown to be sites for fatigue crack initiation [41]. Kung et al. [42] investigated the role of constitutional phases on fatigue cracking at room temperature in detail using notched specimens of alloys 2024 and 2124 (2124 is the high-purity variant of alloy 2024 with reduced Fe and Si content; both in the T4 state). They observed that at high stresses, the cracks in both alloys formed at coarse slip bands. At low stresses, nearly all the cracks in the 2024 alloy initiated in the matrix adjacent to the constitutional phases, whereas only half of the cracks in the high-purity 2124 alloy initiated there. The size of the phases determined the probability of crack initiation: phases < 6 μm play hardly any role. They also found that cracks propagate through the constitutional phases but do not

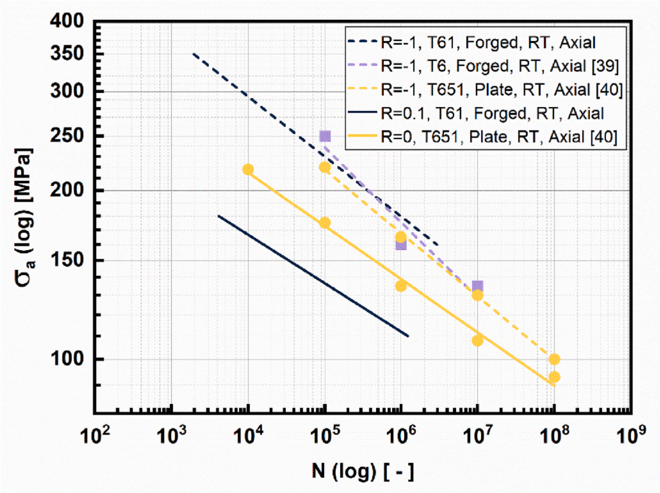

Fig. 11. *Comparison of results with literature data. Stress amplitude* σ_a *vs. no. of cycles* N*. S–N curves from literature data [39,40] plotted using linear regression.*

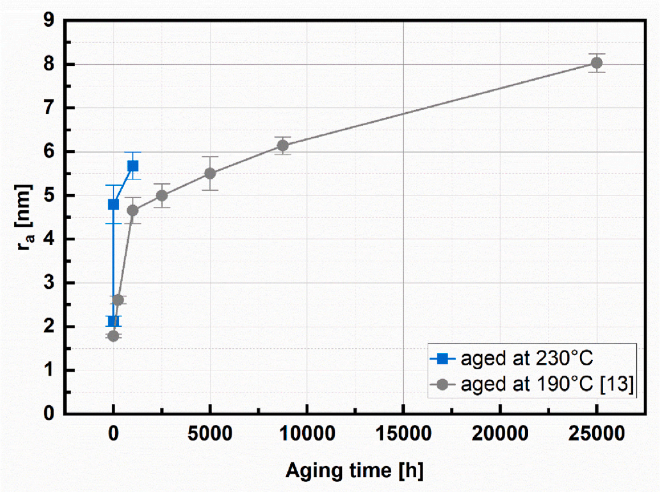

Fig. 12. Average particle radii r_a vs. ageing time. Comparison of average particle radii evolution aged at 230 °C and 190 °C [13] for different aging times. The lines are a guide to the eye for convenience.

form in them or at their interface with the matrix.

Regardless of the material state and stress ratio, primary phases (Al_9FeNi, Mg_2Si) were observed in the crack initiation region in the present study (see section 3.3.2). This suggests that the primary phases may be involved in crack initiation. Similar observations have been made in previous studies [34,42–46], where crack initiation was observed on constituent particles as well as crack initiation on slip bands. However, this was only observed for tests with high stress amplitudes. No slip bands were observed in the specimens tested, neither at low nor at high stress amplitudes. It should be noted that the tested specimens were not as finely polished as in the cited studies.

Ostermann [47] pointed out, that the intermetallic phases bear significant responsibility for the formation of fatigue cracks in engineering aluminum alloys. The different elastic properties of the primary phase and the Al matrix lead to local stress and strain concentrations. These accelerate the attainment of a critical local slip band condition leading to crack initiation. This has been demonstrated by Wisner et al. [48] in their study of particle fracture during fatigue of aluminum alloy 2024. To detect early signs of fatigue damage they combined in-situ scanning electron microscopy with microstructure sensitive nondestructive evaluation using digital image correlation (DIC). High strain concentrations resulting from particle/Al matrix interaction were observed. In some cases, the particles fractured. These fractured particles show localized strains around them, that are 4–5 times higher than the strains within the particles. The study shows a difference in the elastic modulus and hardness for the particle and Al matrix. Based on the results, the authors conclude that the particles act as a stress raiser and the cracks then initiate at these stress concentrations. In addition, crack initiation was observed at fractured particles. In our tests, fractured primary phases were occasionally observed. However, in most cases, crack initiation did not occur at these locations.

Malek et al. [34] performed a comprehensive fatigue study with different load variations (axial, torsional, combined) on 2618. They reported that fatigue cracks developed systematically on coarse primary intermetallic Al_9FeNi particles under all loads investigated. They attributed this to the specific microstructure of 2618 with the very high density of coarse Al_9FeNi particles, which strongly influenced the fatigue behavior. They concluded, that compared to aluminum alloys 2214 or 7050, this even annihilates the surface roughness effect.

The discussion shows that in Al alloys, primary phases and constitutional phases can generally have an impact on crack initiation during fatigue. The alloy design of 2618A is based on the deliberate use of the primary phases Al_9FeNi to achieve sufficient creep resistance. Thus, the primary phases cannot be eliminated and its possible negative effects on fatigue life must be accepted.

5. Conclusion

The influence of mean stress and overaging on the fatigue life of 2618A was investigated. Tests were performed at different stress ratios ($R = 0$, $R = 0.1$) on the initial T61 and on two overaged states (10 h/230 °C, 1000 h/230 °C). Fractography was performed to gain a better understanding of the failure mode and TEM was used to characterize the size evolution of the S-phase. The main results can be summarized as follows:

- Influence of overaging: The average particle radius of the S-phase gradually increases by more than a factor of two after 10 h or after 1000 h of aging. This results in a deterioration in strength (and hardness) and hence to a shorter fatigue life compared to the initial T61 state.
- The failure mode of the T61 state is independent of the stress ratio. There also is no dependency between failure mode and overaging for the tests performed at stresses below the proof strength.
- In most cases, cracks preferentially initiate in the vicinity of primary phases on the outer surface. The reason for this could be the different elastic properties of the primary phases and the Al matrix, leading to local stress and strain concentrations.

CRediT authorship contribution statement

Ying Han: Investigation, Visualization, Writing – original draft, Writing – review & editing. **Julius Kruse:** Investigation, Writing – review & editing. **Julian M. Rosalie:** Investigation, Writing – review & editing. **Jan Radners:** Investigation, Writing – review & editing. **Philipp von Hartrott:** Conceptualization, Writing – review & editing, Supervision, Project administration, Funding acquisition. **Birgit Skrotzki:** Conceptualization, Writing – review & editing, Supervision, Project administration, Funding acquisition.

Declaration of competing interest

The authors declare that they have no known competing financial interests or personal relationships that could have appeared to influence the work reported in this paper.

Data availability

Data will be made available on request.

Acknowledgements

The authors kindly acknowledge Mauro Madia for providing test equipment and for the helpful and inspiring scientific exchange. Special thanks are given to Quynh Hoa Le for the fractographic investigations, Christine Krimmling for performing the hardness measurements and Steffen Thärig for the light microscopic investigations. In addition, the authors would like to thank the company OTTO FUCHS KG for providing the alloy. This research project was funded by the German Federal Ministry for Economic Affairs and Climate Action (BMWK) and the AiF (German Federation of Industrial Research Associations eV) (IGF No. 20850 N). The authors gratefully acknowledge the support received from the funding organizations, from the FVV e.V. and from all those involved in the project.

References

[1] I.J. Polmear, Light Alloys - from Traditional Alloys to Nanocrystals, 4 ed., Elsevier/Butterworth-Heinemann, Oxford; Burlington, MA, 2006.
[2] I.N.A. Oguocha, S. Yannacopoulos, Y. Jin, The structure of AlxFeNi phase in Al-Cu-Mg-Fe-Ni alloy (AA2618), J. Mater. Sci. 31 (21) (1996) 5615–5621.
[3] F. Nový, M. Janeček, R. Král, Microstructure changes in a 2618 aluminium alloy during ageing and creep, J. Alloys Compd. 487 (1) (2009) 146–151.
[4] I.N. Khan, M.J. Starink, J.L. Yan, A model for precipitation kinetics and strengthening in Al–Cu–Mg alloys, Mater. Sci. Eng., A 472 (1) (2008) 66–74.
[5] S.C. Wang, M.J. Starink, N. Gao, Precipitation hardening in Al–Cu–Mg alloys revisited, Scripta Mater. 54 (2) (2006) 287–291.
[6] T.S. Parel, S.C. Wang, M.J. Starink, Hardening of an Al–Cu–Mg alloy containing Types I and II S phase precipitates, Mater. Des. 31 (2010) S2–S5.
[7] G. Liu, G.J. Zhang, X.D. Ding, J. Sun, K.H. Chen, Modeling the strengthening response to aging process of heat-treatable aluminum alloys containing plate/disc- or rod/needle-shaped precipitates, Mater. Sci. Eng., A 344 (1) (2003) 113–124.
[8] B. Heying, R.-D. Hoffmann, R. Pöttgen, Structure refinement of the S-phase precipitate MgCuAl2, Z. Naturforsch. B Chem. Sci. 60 (5) (2005) 491–494.
[9] S.C. Wang, M.J. Starink, Precipitates and intermetallic phases in precipitation hardening Al–Cu–Mg–(Li) based alloys, Int. Mater. Rev. 50 (4) (2005) 193–215.
[10] M.A. Meyers, K.K. Chawla, Mechanical Behavior of Materials, 2 ed., Cambridge University Press, Cambridge, 2008.
[11] J. Wang, D. Yi, X. Su, F. Yin, Influence of deformation ageing treatment on microstructure and properties of aluminum alloy 2618, Mater. Char. 59 (7) (2008) 965–968.
[12] E.M. Elgallad, P. Shen, Z. Zhang, X.G. Chen, Effects of heat treatment on the microstructure and mechanical properties of AA2618 DC cast alloy, Mater. Des. 61 (2014) 133–140.
[13] C. Rockenhäuser, C. Rowolt, B. Milkereit, R. Darvishi Kamachali, O. Kessler, B. Skrotzki, On the long-term aging of S-phase in aluminum alloy 2618A, J. Mater. Sci. 56 (14) (2021) 8704–8716.
[14] I.M. Lifshitz, V.V. Slyozov, The kinetics of precipitation from supersaturated solid solutions, J. Phys. Chem. Solid. 19 (1) (1961) 35–50.

[15] C. Wagner, Theorie der Alterung von Niederschlägen durch Umlösen (Ostwald-Reifung), Zeitschrift für Elektrochemie, Berichte der Bunsengesellschaft für physikalische Chemie, 1961.

[16] G.R. Speich, R.A. Oriani, Rate of coarsening of copper precipitate in an alpha-iron matrix, Trans. Metall. Soc. AIME 233 (4) (1965) 623. &.

[17] C. Rockenhäuser, S. Schriever, P. von Hartrott, B. Piesker, B. Skrotzki, Comparison of long-term radii evolution of the S-phase in aluminum alloy 2618A during ageing and creep, Mater. Sci. Eng., A 716 (2018) 78–86.

[18] G. Malakondaiah, P. Rama Rao, Influence of prior treatment on high strain fatigue life of aluminium alloy RR58, in: D.M.R. Taplin (Ed.), Advances in Research on the Strength and Fracture of Materials, Pergamon, Amsterdam, 1978, pp. 741–747.

[19] V. Singh, M.S.N. Rao, P. Rama Rao, Effect of prior treatment on the low cycle fatigue behaviour of aluminium alloy RR58 at 423K, Int. J. Fatig. 2 (1) (1980) 12–22.

[20] J.M. Finney, Relationship between aged structure and the fatigue behaviour of aluminium-copper-magnesium alloys, Mater. Sci. Eng. 6 (1) (1970) 55–65.

[21] W. Hesse, Key to Aluminium Alloys, 13 ed., Beuth Verlag GmbH, Berlin, 2021.

[22] J.R. Heath-Smith, F.E. Kiddle, Effects of Heat on Fatigue in Aircraft Structure, Procurement Executive Ministry of Defence, Aeronautical Research Council, Reports and Memoranda, London, 1977.

[23] DIN EN 573-3, Aluminium and Aluminium Alloys - Chemical Composition and Form of Wrought Products - Part 3: Chemical Composition and Form of Products, Beuth Verlag GmbH, 2022-09.

[24] DIN EN ISO 7500-1, Metallic Materials - Calibration and Verification of Static Uniaxial Testing Machines - Part 1: Tension/compression Testing Machines - Calibration and Verification of the Force-Measuring System, Beuth Verlag GmbH, 2018-06.

[25] ISO 23788, Metallic Materials - Verification of the Alignment of Fatigue Testing Machines, International Organization for Standardization, 2012-07.

[26] DIN 50100, Load Controlled Fatigue Testing - Execution and Evaluation of Cyclic Tests at Constant Load Amplitudes on Metallic Specimens and Components, Beuth Verlag GmbH, 2022-12.

[27] ISO 1099, Metallic Materials-Fatigue Testing-Axial Force-Controlled Method International Organization for Standardization, 2017-06.

[28] DIN EN ISO 6506-1, Metallic Materials - Brinell Hardness Test - Part 1: Test Method, Beuth Verlag GmbH, 2015-02.

[29] DIN EN ISO 6892-1, Metallic Materials - Tensile Testing - Part 1: Method of Test at Room Temperature, Beuth Verlag GmbH, 2020-06.

[30] DIN EN ISO 9513, Metallic Materials - Calibration of Extensometer Systems Used in Uniaxial Testing, Beuth Verlag GmbH, 2013-05.

[31] J. Aitchison, J.A.C. Brown, The Lognormal Distribution, Cambridge University Press, Cambridge, England, 1957.

[32] C. Rockenhäuser, B. Skrotzki, Zenodo, in: Radii of S-phase Al2CuMg in Al-Alloy EN AW-2618A after Different Aging Times at 190°C, 2023.

[33] DIN EN ISO 643, Steels - Micrographic Determination of the Apparent Grain Size, Beuth Verlag GmbH, 2020-06.

[34] B. Malek, C. Mabru, M. Chaussumier, Fatigue behavior of 2618-T851 aluminum alloy under uniaxial and multiaxial loadings, Int. J. Fatig. 131 (2020), 105322.

[35] S. Suresh, Fatigue of Materials, 2 ed., Cambridge University Press, Cambridge, 1998.

[36] W.D. Callister, D.G. Dethwisch, Materials Science and Engineering: an Introduction, 10 th ed., John Wiley & Sons, United States of America, 2018.

[37] W.F. Hosford, Mechanical Behavior of Materials 2ed, Cambridge University Press United States of America, 2010.

[38] T. Mann, The influence of mean stress on fatigue crack propagation in aluminium alloys, Int. J. Fatig. 29 (8) (2007) 1393–1401.

[39] U. Günther, W. Fessenmayer, O. Krämer, H. Mauch, Untersuchungen zum Einfluss der durch moderne Fräsverfahren gefertigten technischen Oberflächen auf die Ermüdungsfestigkeit, Frankfurt/M., 2001, p. 120.

[40] J.G. Kaufman, Properties of Aluminum Alloys: Fatigue Data and the Effects of Temperature, Product Form, and Processing, 2008.

[41] E.A. Starke, Fatigue of aluminum alloys, in: K.H.J. Buschow, R.W. Cahn, M. C. Flemings, B. Ilschner, E.J. Kramer, S. Mahajan, P. Veyssière (Eds.), Encyclopedia of Materials: Science and Technology, Elsevier, Oxford, 2001, pp. 2946–2950.

[42] C.Y. Kung, M.E. Fine, Fatigue Crack initiation and microcrack growth in 2024-T4 and 2124-T4 aluminum alloys, Metall. Trans. A 10 (5) (1979) 603–610.

[43] R.J.H. Wanhill, Fatigue Crack Initiation in Aerospace Aluminium Alloys, Components and Structures, 2007. Amsterdam.

[44] A.S. Zamarripa, C. Pinna, M.W. Brown, M.P.G. Mata, M.C. Morales, T.P. Beber-Solano, Identification of modes of fracture in a 2618-T6 aluminum alloy using stereophotogrammetry, Mater. Char. 62 (12) (2011) 1141–1150.

[45] A. Merati, A study of nucleation and fatigue behavior of an aerospace aluminum alloy 2024-T3, Int. J. Fatig. 27 (1) (2005) 33–44.

[46] D. Sigler, M.C. Montpetit, W.L. Haworth, Metallography of fatigue crack initiation in an overaged high-strength aluminum alloy, Metall. Trans. A 14 (4) (1983) 931–938.

[47] F. Ostermann, Anwendungstechnologie Aluminium, Springer Vieweg, Berlin Heidelberg, 2014.

[48] B. Wisner, A. Kontsos, Investigation of particle fracture during fatigue of aluminum 2024, Int. J. Fatig. 111 (2018) 33–43.